A Scratch Intersection Model of Material Removal During Chemical Mechanical Planarization (CMP)

Wei Che

Yongjin Guo

Abhijit Chandra[1]
e-mail: achandra@iastate.edu

Department of Mechanical Engineering,
Iowa State University,
Ames, IA 50011

Ashraf Bastawros[2]
Department of Aerospace Engineering,
Iowa State University,
Ames, IA 50011
e-mail: bastaw@iastate.edu

A scratch intersection based material removal mechanism for CMP processes is proposed in this paper. The experimentally observed deformation pattern by SEM and the trends of the measured force profiles (Che et al., 2003) reveal that, for an isolated shallow scratch, the material is mainly plowed sideway along the track of the abrasive particle with no net material removal. However, it is observed that material is detached close to the intersection zone of two scratches. Motivated by this observation, it is speculated that the deformation mechanism changes from ploughing mode to shear-segmentation mode as the abrasive particle approaches the intersection of two scratches under small indentation depth for ductile metals. The proposed mechanistic material removal rate (MRR) model yields Preston constant similar to those observed experimentally for CMP processes. The proposed model also reveals that the nature of the slurry-pad interaction mechanism, and its associated force partitioning mechanism, is important for determining the variation of MRR with particle size and concentration. It is observed that under relatively soft pads, small particles and low particle concentration, the pad undergoes local deformation, yielding an increased MRR with increasing particle size and concentration. At the other extreme, the intact walls of the surface cells and the connecting cell walls between the surface pores deform globally, resembling a beam or a plate, and a decreasing trend in MRR is observed with increasing particle size and concentration. The predicted MRR trends are compared to existing experimental observations. [DOI: 10.1115/1.1949616]

1 Introduction

Precision finishing and planarization are becoming integral process steps in multilevel metallization designs for integrated circuit (IC) manufacturing. This is needed to ensure local and global surface planarization before the next layer is deposited. The surface finishing process [industrially known as Chemical-Mechanical Polishing (CMP)] employs micro and nanoabrasive particles in chemically active slurry with a soft polishing pad to remove material from the surface. In common CMP processes, material removal is accomplished by pressing a wafer into a relatively soft porous pad flooded with an abrasive slurry, while both the pad and the wafer have a relative orbital motion (Fig. 1). The wafer rests on a backing plate, which is rotating about its own axis, and is pressed down against the pad, which is attached to a rotating platen disk. An abrasive slurry with various process specific chemical compounds is typically used in a CMP process. The chemical aspects of the process are thought to be softening and/or dissolving the top layer of the surface while mechanically removing it. Such interaction facilitates usage of soft abrasives in CMP.

This work focuses on understanding the mechanical aspects of the surface material detachment mechanisms during the CMP process. The experimentally observed deformation patterns and force profiles from the microscale scratch experiments [1] are used to provide a plausible mechanism for material detachment through a combination of surface plowing and shearing under the abrasive particles. The gained insights are integrated into mechanism-based models for the material removal rate (MRR).

The process of mechanical surface polishing is usually envisioned through the phenomenological Preston formula [2]; wherein the height reduction rate, is given by:

$$\frac{dh}{dt} = K \cdot P_0 \cdot u \tag{1}$$

and the corresponding volumetric material removal rate (MRR) is given by:

$$\mathrm{MRR} = A_w \cdot \frac{dh}{dt}. \tag{2}$$

Here, P_0 is the applied nominal pressure, u is the relative sliding velocity, A_w is the wafer surface area, and K is the Preston proportionality constant (encompassing the chemical effects). All the unforeseen process parameters are lumped into the proportionality constant. Detailed analysis [3–6] have shown that the pressure dependence is non-linear with exponent that ranges from 0.33 to 1.5 based on the details embraced by the models. These models use a proportionality constant similar to Preston constant to scale the magnitude of model predictions to experimental measurements. Currently, no complete physical basis is attached to the Preston constant. The framework of these polishing models assumes that each active particle under the applied load generates a continuous trench, and the material removed is equivalent to the volume of the generated trench. Such framework is applicable at the macro scale and is in agreement with the conventional card model used in metal cutting and coarse grinding operation [7].

However, for oblique cutting with high negative rake angle, it has been observed by [1] that the local deformation and the nanoscale material removal mechanisms for ductile materials (e.g., copper) are quite different from what is commonly observed in macro scale processes. At these very small "depth of cut," the abrasive particle forms a continuous trench, but the material is not detached from its parent surface. It merely flows from the bottom of

[1]Also at the Department of Aerospace Engineering, Iowa State University.
[2]Also at the Department of Mechanical Engineering, Iowa State University.

Contributed by the Manufacturing Engineering Division for publication in the ASME JOURNAL OF MANUFACTURING SCIENCE AND ENGINEERING. Manuscript received July 21, 2003; final revision received October 12, 2004. Associate Editor: Y. L. Yao.

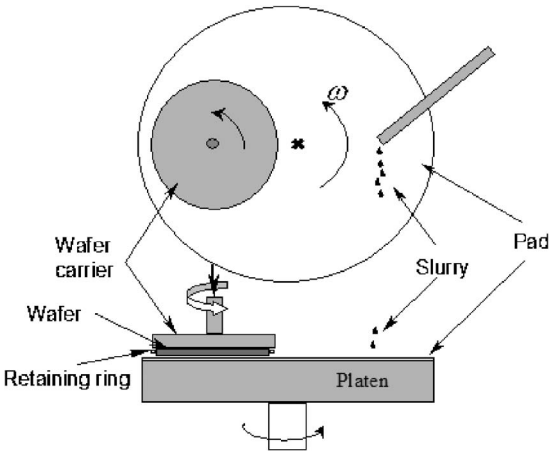

Fig. 1 Schematic diagram of a CMP process

the trench to the side via stable plastic deformation and form "pile up." Such deformation pattern has been observed (as shown in Fig. 2 from an AFM scan) in micro scale scratching of copper [1,8], nanoscale AFM indentation and scratch tests [9], and is akin to profile rolling of gears [10,11]. It is further hypothesized that detachment occurs later as a result of plastic instability due to

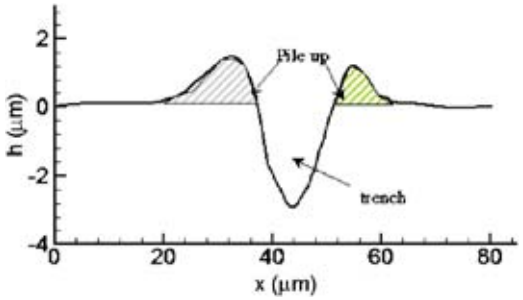

Fig. 2 An AFM scan of a representative scratch cross section during single grit scratching of copper (depth of cut 3 μm). The volume in the trench is about the same as the pile-up volume.

interaction of scratches. This interaction may be in the form of intersection of two scratches or may be due to the vicinity of two parallel scratch-tracks [12]. It can also result from metal fatigue due to repeated plastic deformation in the pile-up region beside the trenches produced by the abrasive particles. Che et al. [1] have investigated only a particular form of this interaction (orthogonal intersection) and established a "*characteristic detachment ratio*" (CDR), which is ratio of the detached material segment at an intersection relative to the depth of cut. In their model formulation, Che et al. [1] assume that the cross section is dictated by the indenter or abrasive particle profile. However, no experimental study investigating the relationship of scratch characteristics (e.g., aspect ratio) to the width of the detached flake has been carried out.

The present paper extends this concept of scratch intersection by employing the characteristic detachment ratio to develop a phenomenological MRR model during the CMP process of annealed copper. The model development steps are given in Sec. 2. The model predictions showing the various domains of MRR are given in Sec. 2.7. Section 3 provides comparison of the model prediction with documented experimental measurements. The discussion and concluding remarks follow in Sec. 4. Throughout the paper, the subscript p stands for pad, w for wafer, a for asperity, and c for the abrasive cutting particles.

2 Material Removal Model Development

To predict the MRR for a CMP process, the transfer of the applied pressure to individual abrasive particle has to be characterized. Following the approach of Luo and Dornfeld [3] and Bastawros et al. [5], a flow chart for analyzing the MRR in a CMP process is schematically shown in Fig. 3. Each step is elaborated in the following sections.

2.1 Determination of the Average Local Pressure Per Asperity. Generally, there are four classifications of pad response ranging from soft to hard according to their surface properties [13]. Hard pad is ideal for global planarization and reduction of the dishing problem, but it may cause some surfaces defects like scratches. Soft pad is good for reducing surface defects, but prone to the dishing problem. Accordingly, there is a trade off in selecting the pad for a Cu-CMP process. The topography structure of a frequently used IC1000 (relatively soft pad) is shown in Fig. 4 [5].

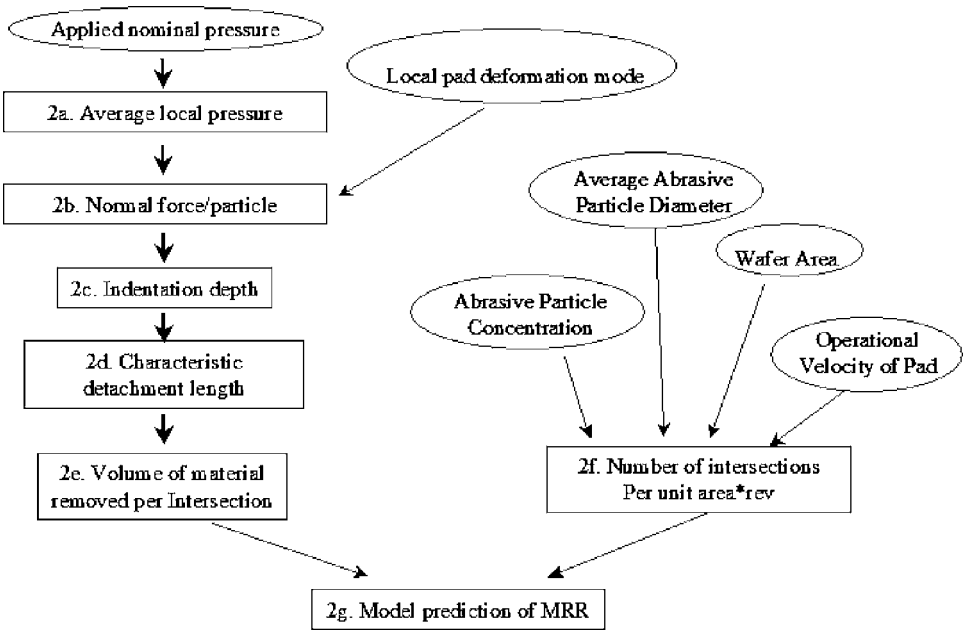

Fig. 3 Flow chart for calculating the MRR in a typical CMP process

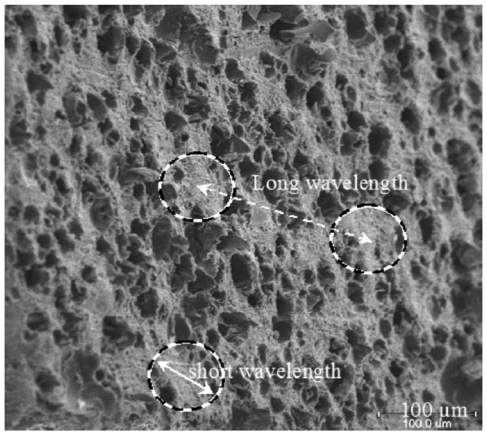

Fig. 4 SEM image of an IC1000 pad. The pad surface is tilted 60 deg of the viewing axis to show the relative surface topography. The average pore diameter is about d_p=50 μm.

The average pore diameter is about 50 μm, and the pad surface density is about 35%. The analysis of pad surface roughness has shown the existence of multiple wavelength roughness. A long wavelength is observed with length scale about 15–20 times the pore diameter, with amplitude about 0.1–0.2 times the pore diameter. Within this long wavelength, there are clusters of pad asperities of about 2–4 times the cell diameters. The short wavelength of the local cell surface roughness is about 1–2 μm. Accordingly, the applied nominal pressure is supported by the high regions (or asperities) of the pad, which is in contact with the wafer surface. Since the typical abrasive particle diameter is of the order of 100 nm, only those particles residing on the high regions of the pad are active in cutting the wafer surface material. Therefore, the local contact pressure between the pad asperities and the wafer surface has to be estimated.

A simple model is developed to describe this relationship based on the force equilibrium. Following the approach of Luo and Dornfeld [3], Bastawros et al. [5] and Seok et al. [6], a periodic roughness with number of asperities per unit area, ρ_a, over the pad surface is assumed. ρ_a is a characteristic of the pad surface topography. As a first approximation, we will consider that ρ_a does not evolve with pad deformation and wear. Accordingly, the normal force per asperity will be:

$$F_a = \frac{P_0}{\rho_a} \tag{3}$$

The long wavelength asperities are assumed to have a radius of curvature R_a. The evolution of the contact area between the asperity and the wafer surface is represented by Hertzian elastic contact. In this model the asperity is assumed to be deformable while the wafer surface is assumed to be relatively rigid. Accordingly, the contact radius a is given as a function of P_0 by

$$a = \left[\frac{3}{4}\frac{P_0 R_a}{\rho_a E}\right]^{1/3} \tag{4}$$

and

$$\frac{1}{E} \equiv \frac{1-\nu_w^2}{E_w} + \frac{1-\nu_p^2}{E_p} \approx \frac{1}{\bar{E}_p} \tag{5}$$

Here E is the equivalent elastic modulus, E_w, E_p, ν_w, and ν_p are the elastic moduli and Poisson's ratio of the wafer and the porous pad respectively, and $\bar{E}_p = E_p/(1-\nu_p^2)$. Accordingly, each pad asperity will have a summit with an area, $A_a = \pi a^2$. The total wafer/pad contact area is given by the total number of asperities and the area of each asperity

$$A \equiv (\rho_a A_w) A_a = \lambda A_w \left(\frac{P_0}{\bar{E}_p}\right)^{2/3}$$

$$\lambda = \pi\left[\frac{3}{4} R_a \sqrt{\rho_a}\right]^{2/3} \tag{6}$$

where λ is a dimensionless parameter that represents the pad surface topography. λ is about 0.6 for the IC1000 pad based on Bastawros et al. [5] definition of contact area ration $A/A_w = \pi\beta(R_a/\lambda)^2$, wherein β is the pad surface density of about 35%. From force equilibrium as illustrated in Figs. 5(*a*) and 5(*b*), the average local pressure at the asperity level is given by

$$P \equiv \frac{P_0 \cdot A_w}{A} = \frac{\bar{E}_p^{2/3} P_0^{1/3}}{\lambda} \tag{7}$$

The assumptions implied so far are similar to those of Hertz elastic contact model, and the pad surface roughness has a nonevolving periodic asperities. It is also assumed that the pres-

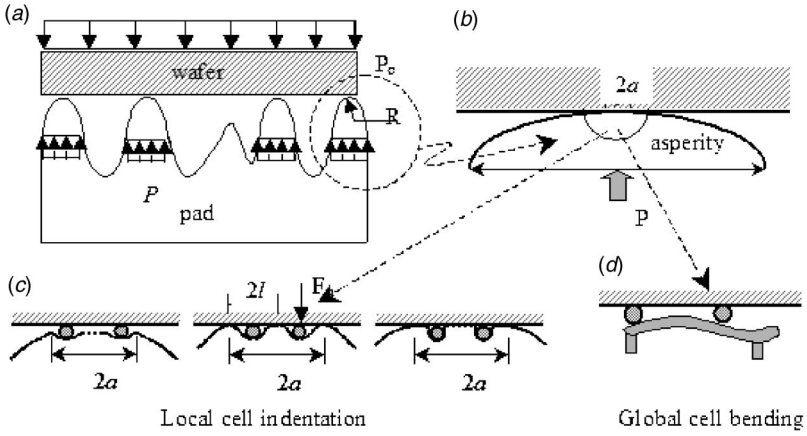

Fig. 5 Schematic representation of the multiscale of the wafer/pad contact. (*a*) Long wavelength multi asperity contact; (*b*) details of individual pad asperity contact under local pressure, *P*; (*c*, *d*) cell level deformation as a local indentation (with no, partial, or full contact of the wafer/pad interface); (*d*) bending of the entire cell.

sure at the asperity level is represented by an equivalent uniform local pressure, instead of the actual local pressure distribution over each asperity.

2.2 Determination of the Normal Force Per Particle. At the scale of the abrasive particle, Fig. 5 shows that the load is carried out either by the wafer/pad or wafer/particle/pad contact. Locally, two deformation mechanisms can be identified and primarily linked to the pad structure based on (I) local cell indentation by individual abrasive particles as depicted in Fig. 5(*c*) [5,14], and (II) by overall cell bending as depicted by Fig. 5(*d*) [4]. Based on these two deformation modes, we have identified four deformation mechanisms. Mechanisms (i)–(iii) are associated with local cell indentation and (iv) is associated with overall cell bending.

Local cell indentation depicted in Fig. 5(*c*) is usually associated with soft porous pads similar to the IC1000 pad, wherein the abrasive particle progressively indents the pad surface cells. Deformation mechanism (i) represents the initial state of the wafer pad interaction, wherein the pad and wafer will not come to contact. Mechanism (ii) corresponds to the establishment and evolution of partial pad/wafer contact, wherein each abrasive particle forms the shown "hut" shape over the pad surface. Mechanism (iii) corresponds to the final hypothetical state of a very soft pad or very low slurry concentration, wherein the pad fully enclaves the abrasive particles and comes to full contact with the wafer. Alternatively, Fig. 5(*d*) depicts deformation mechanisms (iv) associated with a fibrous pad like the TWP817 pad, wherein the cells or fibers globally bend around the abrasive particles. This deformation mode can associate with the porous IC1000 pad if the surface cell thickness are small and large abrasive particles are employed (approximately μm range). More detailed discussion of the combination of different pad deformation modes is given in Gouda et al. [14]. These modes of deformation dictate the average local pressure within the long wavelength pad asperities, and the imparted normal forces on individual abrasive particles. The force per particle will be calculated for both modes of deformation as follows.

For mechanism (i) of local pad deformation and no established wafer/pad contact, all the applied pressure will be carried out by the particles within the contact area of the asperity. The slurry is assumed to have an average particle size of diameter d, and a homogeneous volumetric concentration α. If the height of the gap between the pad asperities and the wafer is assumed to be the average particle diameter d [15], then the number of particles that is in contact with the wafer can be given by:

$$N_{\text{partical}} \equiv \frac{\alpha A d}{\pi\, d^3/6} = \frac{6\alpha A}{\pi\, d^2} \tag{8}$$

Accordingly, by employing Eq. (5) for the local pressure P within individual asperity, then the force per particle F_n will be

$$F_n \equiv \frac{P \cdot A}{N_{\text{partical}}} = \frac{\pi}{6} \cdot \frac{\bar{E}_p^{\,2/3}}{\lambda} \cdot \frac{d^2}{\alpha} \cdot P_0^{\,1/3} \tag{9}$$

For mechanism (ii) of partial pad/particle/wafer contact, it can be assumed that the normal force per particle is simply the product of the contact pressure between the pad and the particle and the suspended area of the "hut." Based on this assumption and the FEM results of Bastawros et al. [5] for the IC1000 pad, the normal force F_n on an individual particle is given by

$$F_n = \frac{\pi}{4} \xi_3 P l^2 \tag{10}$$

where $\xi_3 \approx 1.55$ is a geometric factor used to account for the difference in pressure distribution at the edge in the FEM model ([5], dashed line in their Fig 4). The suspended radius l of the "hut" is given by Bastawros et al., [5],

$$l = d\xi_2 \left(\frac{P}{E_p^*} \right)^{-m} \tag{11}$$

where $\xi_2 \approx 1.22$, $m \approx 0.38$, are also proportionality and exponent constants respectively, used to represent the power law relation between average local pressure P and the suspended radius l of the "hut" made by the particle in FEM simulation. E_p^* is the elastic modulus of dense pad material (i.e., the modulus of dense polyurethane $\sim$1.7 GPa). Accordingly, F_n will be

$$\begin{aligned} F_n &= \frac{\pi}{4} \xi_3 \left(\frac{\bar{E}_p^{\,2/3} P_0^{\,1/3}}{\lambda} \right) \left(d^2 \xi_2^2 \left(\frac{\bar{E}_p^{\,2/3} P_0^{\,1/3}}{\lambda E_p^*} \right)^{-2m} \right) \\ &= \frac{\pi\, \xi_2^2 \xi_3}{4} \cdot \frac{E_p^{\,(2/3)(1-2m)} E_p^{*2m}}{(\lambda)^{1-2m}} \cdot d^2 \cdot P_0^{\,(1/3)(1-2m)} \end{aligned} \tag{12}$$

For mechanism (iii) of full pad/particle/wafer contact, the noncontact domain length $2l$ approaches the particle diameter d. Such a mode has been adopted by Luo and Dornfeld [3], Seok et al. [6] and shown by Bastawros et al. [5] as the limiting case of mechanisms (ii). The normal force per particle is given by

$$F_n \equiv \frac{\pi}{4} d^2 P = \frac{\pi}{4} \cdot \frac{\bar{E}_p^{\,2/3}}{\lambda} \cdot d^2 \cdot P_0^{\,1/3} \tag{13}$$

For mechanisms (iv) where the pad surface cells or fibers globally bend around the abrasive particles, the cell level deformation can be approximated by bending of a beam or a plate as depicted in Fig. 5(*d*). For this mechanism, Fu et al. [4] has given the normal force per particle to be:

$$F_n = \left(\left(\frac{4}{3} \right)^5 E_p^* \cdot T_p^3 \cdot \frac{d}{2} \cdot \left(\frac{A}{N_{\text{partical}}} \right)^2 \cdot P^3 \right)^{1/4}. \tag{14}$$

Here T_p is the pad cell wall thickness. Utilizing Eq. (11) for the A/N_{partical} ratio, and Eq. (7) for P, then F_n can be expressed as:

$$F_n = \left(\frac{2}{3} \right)^{7/4} \sqrt{\pi} \cdot \frac{T_p^{3/4} \cdot E_p^{*1/4} \cdot \bar{E}_p^{1/2}}{\lambda^{3/4}} \cdot \frac{d^{5/4}}{\sqrt{\alpha}} \cdot P_0^{1/4}. \tag{15}$$

Each of the equations for F_n includes three parameter groups. Aside from a scaling factor, the first parameter depends on the pad morphology and elastic modulus. The second group represents the slurry properties and the third is the applied nominal pressure. These groups of parameters can be further expanded to include the stochastic of the process as manifested in particle size distribution and pad surface asperity distribution.

2.3 Determination of Indentation Depth of a Single Abrasive Particle. Once the force per particle is known from the different local pad deformation mechanism, grove depth on the wafer surface can be estimated. First, we assume that the chemical reaction in a CMP process creates a "*chemical product*" layer on the wafer surface that can be modeled as a perfectly plastic material. Following Fu et al. [4] to establish the force equilibrium at the particle-wafer interface, the indentation depth can be estimated as

$$h = \frac{F_n}{\pi \cdot \sigma_y \cdot d} \tag{16}$$

where σ_y is yield strength of material in the chemically reacted layer (taken as equivalent yield strength) and d is the diameter of the spherical abrasive particle.

2.4 Estimation of the Characteristic Detached Length, l_c During Scratch Intersection. In our previous work [1] for the microscratch experiment, it has been shown that the deformation ahead of a moving indenter changes from plowing mode into a shear segmentation mode, triggered by plastic instability near an intersecting scratch. The experiments were carried out on oxygen free, 99.99% high purity copper disks with a 90 deg included angle conical indenter. The scratch depth is in the range of

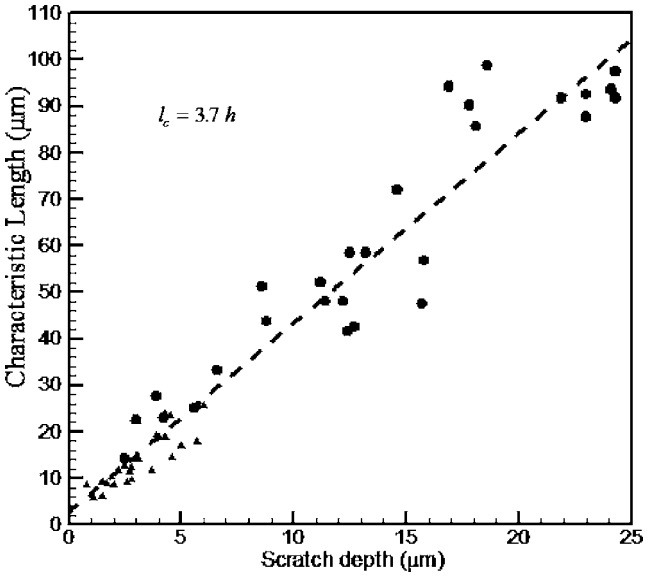

Fig. 6 Characteristic detachment length variation with the scratch depth

1–30 μm. The length of the sheared segment l_c is consistently measured for all tested cases and is plotted in Fig. 6 against the scratch depth, h at the point of intersection. It is found that the CDR is about 3.7. Using a statically admissible state of stress as that shown in Fig. 7 under the indenter for a 2D orthogonal cutting with negative rake angle, a simple shear failure criterion is derived. The estimated CDR is found to be 7.6. This higher value of l_c may be due to the approximations involved in comparing results from 3D experiments against a 2D orthogonal cutting theory model. Here, we will use a CDR of 4 for the calculation of the MRR.

2.5 Determination of the Volume of Material Removed in an Intersection. The volume of removed material per intersection will be function of the indenter (or abrasive particle) profile and l_c. For a spherical particle with diameter d, the formed trench will be having a cross-section, A_c in the form of a segment of a circle, as shown in Fig. 8. In CMP, the abrasive particle diameter is about 100 nm or greater, while the indentation depth is within a few nanometers. It can be safely assumed that the contact angle 2θ is

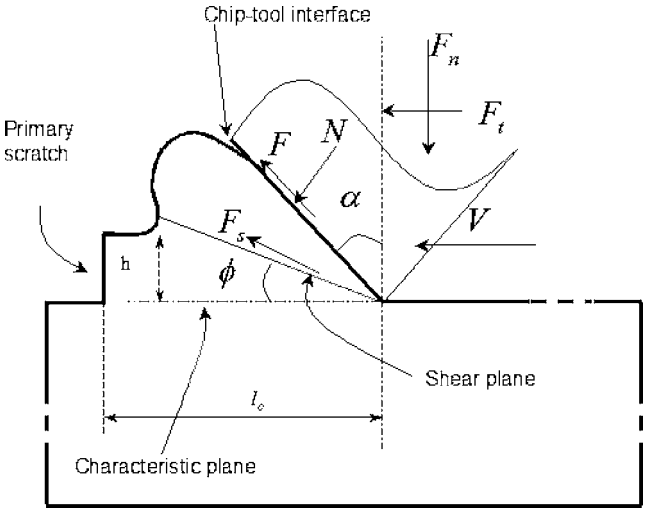

Fig. 7 Schematic of scratch intersection

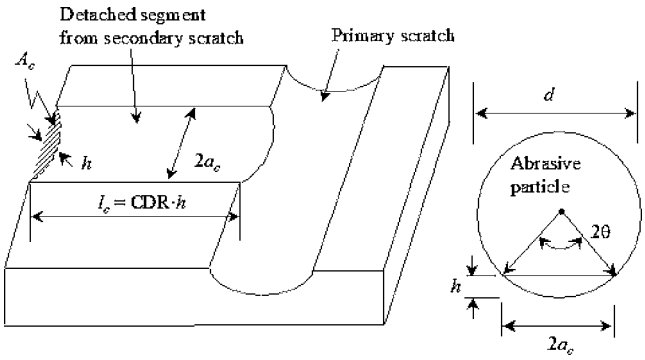

Fig. 8 Schematic of volume of detached flake at intersection

small. Accordingly, $\sin\theta \cong \theta$ and θ may be approximated as $2\sqrt{h/d}$. For small penetration depth h, the radius of the contact impression a_c can be written as

$$a_c = \sqrt{\frac{d^2}{4} - \left(\frac{d}{2} - h\right)^2} \cong \sqrt{dh} \tag{17}$$

and the cross-section area A_c can be written as

$$A_c \cong \tfrac{2}{3} \cdot 2a_c \cdot h = \tfrac{4}{3} h\sqrt{dh} \tag{18}$$

The volume removed per scratch intersection, V_c can be written as

$$V_c \equiv \ell_c \cdot A_c = \mathrm{CDR} \cdot h \cdot \left(\frac{4}{3} h\sqrt{dh}\right) = \tfrac{4}{3}\ \mathrm{CDR}\ h^{2.5} d^{0.5} \tag{19}$$

Employing Eq. (16), V_c can be rewritten as a function of F_n and σ_y

$$V_c = \frac{4}{3\ \pi^{2.5}} \frac{\mathrm{CDR}}{d^2} \left(\frac{F_n}{\sigma_y}\right)^{2.5} \tag{20}$$

It should be noticed that existing MRR models assume that all the material in the trench is removed, and the volume per unit time is taken as the product of A_c with the velocity of the particle. Such an approach is quite different from the intersection model proposed here.

2.6 Determination of the Number of Intersections Per Unit Area Per Revolution. The number of intersections per unit wafer area per revolution of wafer depends on several characteristics of the CMP process. The slurry is assumed to have an average particle size of diameter d, and a homogeneous volumetric concentration α. The linear particles velocity, u relative to the wafer is assumed to be uniform across the entire wafer surface [16]. Moreover, the height of the slurry in the gap between protruding pad asperities and the wafer surface is assumed to be the same as the average particle diameter d [15]. Accordingly, the volume concentration may be represented as a function of the interparticle distance $L_{p\text{-}p}$

$$\alpha = \frac{\pi d^3/6}{L_{p\text{-}p}^2 \cdot d} = \frac{\pi d^2}{6L_{p\text{-}p}^2} \tag{21}$$

Or alternatively,

$$L_{p\text{-}p} = \sqrt{\frac{\pi d^2}{6\alpha}} \tag{22}$$

To derive an evolution equation for the scratch intersection, we will follow the abrasive particles trajectories relative to the wafer and forming the first set of track trajectories at time instant t. Then calculate the time increment Δt needed for the wafer to rotate such that the already formed tracks rotate by an angle β_t to allow for the incoming particles to intersect with the previously formed tracks. Figure 9 is a schematic representation of a wafer being

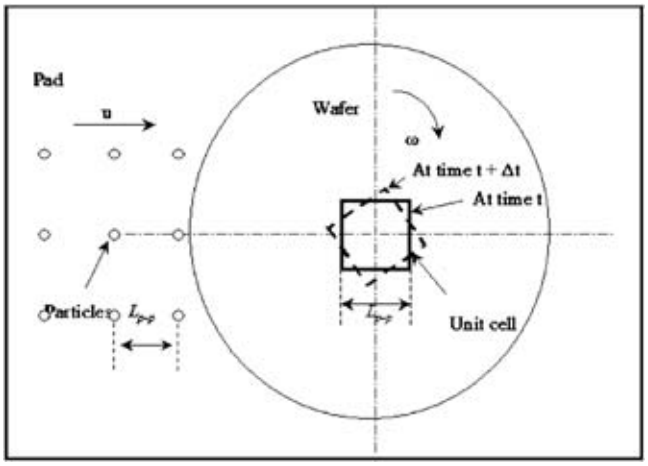

Fig. 9 A schematic of particle motion in the CMP process

polished, showing the relative approach of the abrasive particles into the rotating wafer around its axis. A unit cell with edge length $L_{p\text{-}p}$ at the wafer center is selected at time t, and its rotated new position $t+\Delta t$. By selecting a coordinate axis attached to the wafer, then the unit cell shown in Fig. 10 will see the approaching train of particles with different incident angles. Accordingly, each particle in the approaching train will induce a trench with different angle. And the intersection of all these trenches will contribute to the cumulative MRR. However, when the first particle of the train induce a trench in the unit cell at time t, the following particles in this train will not form a new trench until the separation distance x increases beyond a critical value. When the separating distance exceeds this critical value, the ith particle of train will form a new trench in this unit cell at time $t+\Delta t$. Thus, it is speculated that a new trench is formed only after the wafer rotates by a critical angle of rotation, β_t. Based on this assumption, a simple model is developed to represent the number of intersections per revolution per unit area.

The trailing angle β_t can be approximated by

$$\beta_t = \tan^{-1}\left(\frac{2x}{L_{p\text{-}p}}\right) \tag{23}$$

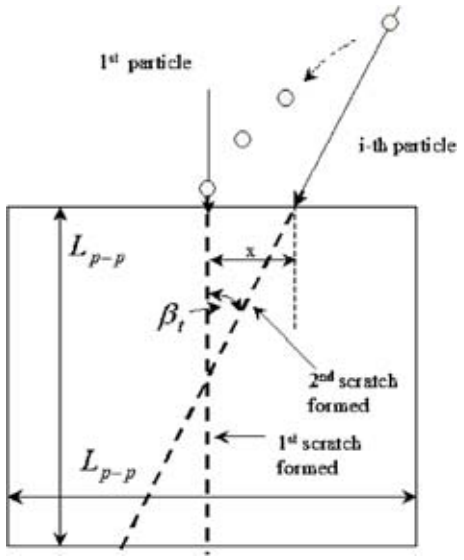

Fig. 10 A schematic of particle train motions relative to the unit cell

A new trench is formed for every β_t angle of rotation. In each full revolution, the number of trenches is

$$N_{\text{rev}} = \frac{2\pi}{\beta_t} \tag{24}$$

Since each pair of the formed trenches may intersect once, then the number of intersections per revolution in this unit cell is given by

$$N_{\text{in-cell}} \equiv C^2_{N_{\text{rev}}} = \frac{N_{\text{rev}}!}{2!\cdot(N_{\text{rev}}-2)!} = \frac{N_{\text{rev}}\cdot(N_{\text{rev}}-1)}{2} = \frac{1}{2}\frac{2\pi}{\beta_t}\cdot\left(\frac{2\pi}{\beta_t}-1\right). \tag{25}$$

Employing Eq. (22) to normalize Eq. (25) by the area of the unit cell, the number of intersections per revolution per unit area, N_{in} is

$$N_{\text{in}} \equiv \frac{N_{\text{in-cell}}}{L^2_{p\text{-}p}} = \frac{6\alpha}{d^2\beta_t}\left(\frac{2\pi}{\beta_t}-1\right) \tag{26}$$

2.7 Estimation of the MRR. Based on our scratch intersection experiment [1], it is more reasonable to apply our new observed material removal mechanism to the MRR model. The MRR is now function of the volume of each scratch intersection V_c, the number of intersection over the percentage of wafer surface that is in contact with the pad $(N_{\text{in}}\cdot A)$, and the rotational speed ω. Accordingly, the rate of height reduction is given by

$$\frac{dh}{dt} \equiv \frac{\text{MRR}}{A_w} = \frac{\omega\cdot(A\cdot N_{\text{in}})\cdot V_c}{A_w} \tag{27}$$

Utilizing Eq. (6) for the contact area ratio, Eq. (20) for V_c and Eq. (26) for N_{in}, then the height reduction rate can be simplified to be:

$$\frac{dh}{dt} = \omega\lambda\left(\frac{P_0}{\bar{E}_p}\right)^{2/3}\left(\frac{6\alpha}{d^2\beta_t}\left(\frac{2\pi}{\beta_t}-1\right)\right)\frac{4}{3\pi^{2.5}}\frac{\text{CDR}}{d^2}\left(\frac{F_n}{\sigma_y}\right)^{2.5} = \frac{8}{\pi^{2.5}}\left\{\frac{\text{CDR}}{\beta_t}\left(\frac{2\pi}{\beta_t}-1\right)\right\}\left\{\frac{\lambda}{\bar{E}_p^{2/3}}\right\}\left\{\frac{\alpha}{d^4}\right\} \times\left\{\frac{1}{\sigma_y}\right\}^{2.5}\cdot\{\omega\cdot P_0^{2/3}\}\cdot F_n^{2.5} \tag{28}$$

The rate of height reduction is explicitly written in terms of five parameter groups, marked by the curly brackets. These groups are as follows: (1) the process kinematics, (2) the pad surface roughness and mechanical properties (E_p,ν_p,λ), (3) the slurry properties (d,α), (4) the mechanical properties of the chemical product layer (σ_y), and (5) the external control parameters (P_0,ω). The remaining term is the force per particle. Its implicit dependence on the whole parameter set is dictated by the local mode of pad deformation at the pad cell level. Such dependence will be shown next as the main source for the various (and sometimes contradictory) experimentally observed trends for the MRR.

Mechanism (i) represents the early stage of pad deformation at relatively low applied pressure. It is especially prevalent for a stiff pad and high particle concentration. At this stage, no direct pad wafer has been established. However, it is believed that this regime is usually rare in a CMP process. For this mechanism, the pad deformation mode is predominantly a cell level local indentation by the abrasive particles. Accordingly, by employing Eq. (9) into Eq. (28), the height reduction is given by

$$\frac{dh}{dt} = \frac{8}{6^{2.5}}\left\{\frac{\text{CDR}}{\beta_t}\left(\frac{2\pi}{\beta_t}-1\right)\right\}\left\{\frac{\bar{E}_p}{\lambda^{1.5}}\right\}\left\{\frac{1}{\sigma_y}\right\}^{2.5}\left\{\frac{d}{\alpha^{1.5}}\right\}\cdot\omega P_0^{1.5}$$

Table 1 MRR model parameters and prediction

CDR	λ	β_t	E_p (MPa)	v_p	σ_y (MPa)	d (nm)	α (vol %)	Predicted K (preston's constant)	Experimental K (preston's constant)
4	0.6	10°	180	0.15	70	100	1.25	~1500	(~1900)

$$\frac{dh}{dt} \propto \frac{d \cdot \omega \cdot P_0^{1.5}}{\alpha^{1.5}} \tag{29}$$

During this mode of local pad deformation and according to Eq. (29), the MRR should be increasing with the increase of the abrasive particle size and reduced particle concentration.

Mechanism (ii) commences upon increasing the applied pressure, wherein partial pad/wafer contact takes place around the local cell indentation zones by the abrasive particles. This mechanism is believed to widely occur during the CMP processes for soft fumed closed pore pads and relatively small abrasive particle sizes (~100 nm). Accordingly, by employing Eq. (12) into Eq. (28), the height reduction is given by

$$\frac{dh}{dt} = \frac{\xi_2^5 \xi_3^{2.5}}{4}\left\{\frac{\mathrm{CDR}}{\beta_t}\left(\frac{2\pi}{\beta_t}-1\right)\right\} \times \left\{\frac{\bar{E}_p^{(1/3)(3-10m)} \cdot E_p^{*5m}}{\lambda^{1.5-5m}}\right\} \cdot \left\{\frac{1}{\sigma_y}\right\}^{2.5} \alpha\, d\, \omega\, P_0^{(1/3)(4.5-5m)} \tag{30}$$

$$\frac{dh}{dt} \propto d \cdot \alpha \cdot \omega \cdot P_0^{0.87} \text{ (for IC 1000 pad)}$$

In contrast to the initial no contact regime. [Eq. (29)], the MRR is now increasing with both the particle diameter and the concentration increases. Moreover, it has a near linear dependence on the applied pressure.

Mechanism (iii) commences at the hypothetical limit where in the pad fully wrap around each abrasive particles and establish contact with the wafer. Accordingly, by employing Eq. (13) into Eq. (28), the height reduction is given by

$$\frac{dh}{dt} = \frac{1}{4}\left\{\frac{\mathrm{CDR}}{\beta_t}\left(\frac{2\pi}{\beta_t}-1\right)\right\}\left\{\frac{\bar{E}_p}{\lambda^{1.5}}\right\}\left\{\frac{1}{\sigma_y}\right\}^{2.5} \alpha\, d\, \omega\, P_0^{1.5} \tag{31}$$

$$\frac{dh}{dt} \propto d \cdot \alpha \cdot \omega \cdot P_0^{1.5}$$

During this mode of pad deformation, the MRR continue to increase linearly with both the abrasive particle diameter and concentration as set by the pervious stage of mechanism (ii). However, it recovers the strong dependence on the pressure as set by mechanism (i).

Mechanism (iv) accounts for the fibrous structure of CMP pads wherein the deformation mode is approximately bending of the strands. Under partial pad/wafer contact and by employing Eq. (15) into Eq. (28), the height reduction is given by

$$\frac{dh}{dt} = 5.68\left\{\frac{\mathrm{CDR}}{\beta_t}\left(\frac{2\pi}{\beta_t}-1\right)\right\} \times \left\{\frac{T_p^{15/8} \cdot \bar{E}_p^{0.583} \cdot E_p^{*5/8}}{\lambda^{7/8}}\right\} \cdot \left\{\frac{1}{\sigma_y}\right\}^{2.5} \left\{\frac{1}{\alpha^{1/4} \cdot d^{7/8}}\right\} \omega P_0^{1.292} \tag{32}$$

$$\frac{dh}{dt} \propto \frac{\omega \cdot P_0^{1.292}}{\alpha^{1/4} \cdot d^{7/8}}$$

For this mode of deformation, the MRR becomes inversely proportional with both the particle sizes and their concentration. However, the pressure dependence remains within the same range.

3 Comparison to Experimental Observations

Examining the different forms of the MRR prediction models indicate variable trends on both the particle size and concentration. In some instances, it could be increasing, decreasing or showing no dependence on these two variables. To show the capability of these set of models, we will compare them next to groups of experimental MRR measurements, gathered from literature under different operating conditions.

3.1 Preston Constant and Variation of MRR With Pressure and Velocity. The first set of experimental results are those of Luo et al. [17] for Cu CMP. These tests were carried out on a Strasbaugh 6CA polisher. The copper-coated wafers (from Silica Source Technology) were used in these experiments. The abrasive particles are α-alumina and γ-alumina particles that are supplied by Universal Photonics. The polishing experiments were performed either with a SUBA IV pad or with a stacked SUBA IV and perforated IC 1000 with IC 1000 on top. The polishing parameters were set 3.5 ml/s slurry flow rate. The downward pressure was varied from 10 to 50 kPa. The rotational speed of table and quill was varied from 15 rev/min(7.2 m/min) to 75 rev/min(35.9 m/min). For the results reported here, an abrasive concentration of 5 wt. %, and mean abrasive size of 100 nm were used.

Since the particle size is relatively small with low concentration, the pad is expected to undergo local deformation for this set of experiments. Thus, the deformation mechanism (ii) is expected to prevail and Eq. (30) will be applied. The estimates of model parameters are shown in Table 1. Pad modulus E_p and v_p is taken for the IC1000 pad [5]. Yield strength of pure copper is taken from the literature. CDR is the proportionality constant for "characteristic detachment ratio" [1]. λ is evaluated to be a constant for the IC 1000 pad. β_t is an estimated value. The predicted K is calculated based on Eq. (30), and experimental K is taken from the experimental data from Luo et al. [17]. It is interesting to notice that the model prediction for Preston constant is about 80% of the measured one, despite the fact that no accurate topology measurements of the utilized pad in this experiment has been done. The reported prediction is based on atypical morphology of a used IC1000 pad for about 1 h of polishing with intermittent conditioning. Moreover, the variation of the local temperature field may also affect the chemical reaction rate, an aspect of the process that has not been addressed here. The current MRR model resemble the form of Preston formula [Eq. (1)] except that the Preston constant is given here by the detailed pad morphology, the ductile film properties, as well as particle sizes and distributions, rather than using it as a fitting parameter.

The model prediction is superimposed on the experimental data in Fig. 11 for the variation of the MRR with applied nominal pressure, at a rotational speed of ω=35 rev/min (corresponds to 16.8 m/min). The variation of the MRR with the relative velocity is shown in Fig. 12, for a down pressure, P_0=30 kPa.

It may be observed from both Figs. 11 and 12 that model predictions of MRR compare well with the experimental data. It should be noted here, that comparisons shown in Figs. 11 and 12 do not involve any "fitting parameter" other than those shown in Table 1.

Since the trailing angle is an estimated value, it is imperative to examine how sensitive the MRR estimates relative to variations in β_t. For the sample calculations shown in Table 1, β_t is taken to be

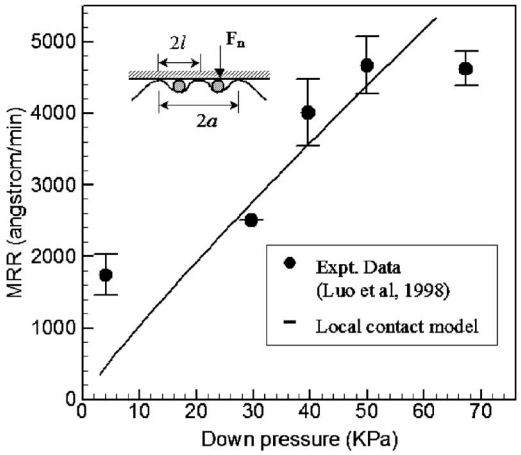

Fig. 11 MRR variation with pressure for copper CMP data

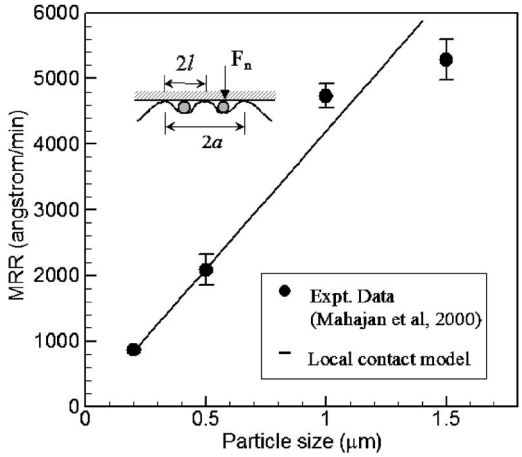

Fig. 13 MRR variation with particle size for a fixed 2 wt. % concentration (SiO_2 CMP)

10 deg as a physically acceptable value to allow three particle diameters spacing before starting new trench. However, if the trailing angle is reduced by 50%, then the ratio of model predicted MRR is about 3 times the experimental MRR. If the trailing angle is increased by 50%, then the model predicted MRR drops to about 1/3 of the experimental MRR data for copper. Accordingly, the choice of $\beta_1 = 10$ deg seems kinematically admissible.

3.2 Variation of MRR With Particle Size and Concentration. By comparing Eq. (30) with Eq. (32), it is interesting to note that the trend of MRR variation with particle size and concentration completely reverses when the pad deformation mode changes from local deformation to global beam mode deformation. Mahajan et al. [18] have investigated the effects of particle size and concentration on the CMP of silicon oxide film for relatively large (0.2–1.5 μm) abrasive particles. These experiments are carried on Struers Rotopol 31 polisher with 7 psi down pressure and a rotational speed of 150 rpm for both the wafer and pad. IC1000 and Suba IV stacked pads (supplied by Rodel, Inc.) are used. The abrasive particles (obtained from Geltech Corporation) have a very narrow particle size distribution, and the particle size and shape are determined by TEM and SEM. They have also varied the particle concentration from 2 wt. % to 15 wt. %. Comparisons of model predictions to their experimental data are presented in Figs. 13–15. Since the required model parameters are not known, especially the yield stress of the hydroxilated layer, the Preston constant is used as a fitting parameter for these comparisons.

The MRR variation with particle size at a relatively low concentration of 2 wt. % is shown in Fig. 13. In this regime, the pad is expected to undergo local deformation, and Eq. (30) is anticipated to apply. It is observed that model predictions from Eq. (30)

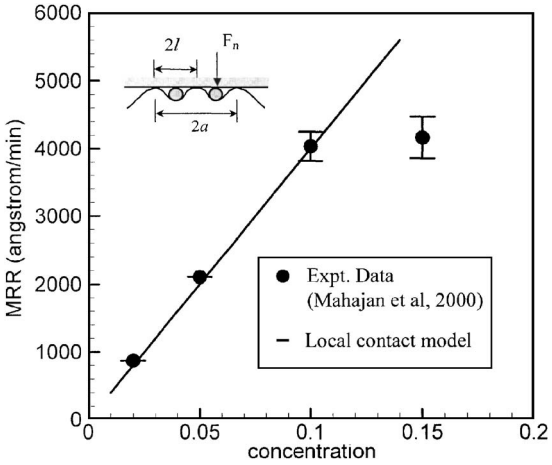

Fig. 14 MRR variation with concentration for particle size of 0.2 μm (SiO_2 CMP)

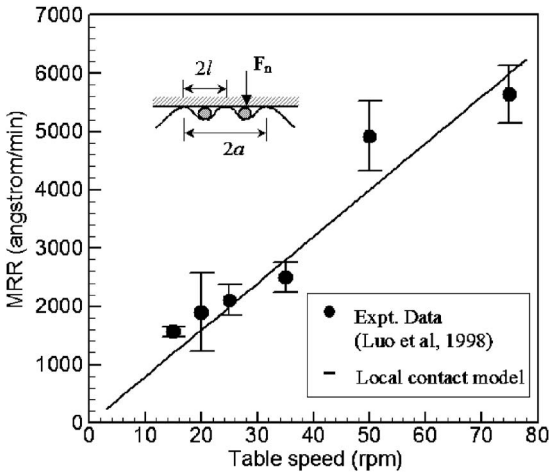

Fig. 12 MRR variation with velocity (copper CMP)

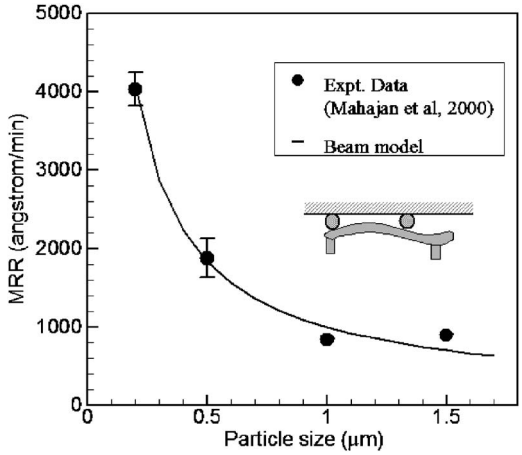

Fig. 15 MRR variation with particle size for a fixed 10 wt % concentration (SiO_2 CMP)

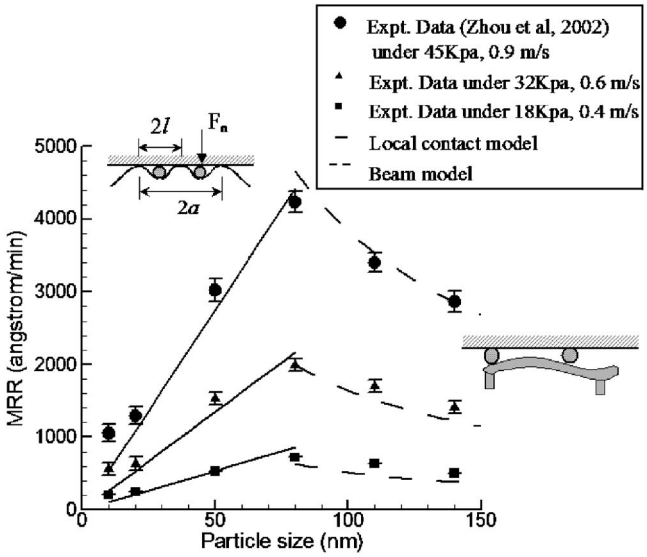

Fig. 16 MRR variation with particle size (SiO_2 CMP)

compare well to the experimental trend. As the abrasive size increases, the pad has a greater tendency to be dominated by cell or strand bending deformation, rather than local surface cell indentation. This mode of deformation would cause the experimental trend to "fall off" the linear trend predicted by Eq. (30). Similarly, Fig. 14 compares the model prediction of Eq. (30) with the observed experimental trend for MRR variation with particle concentration. The comparison is done for a low concentrations ($<15\%$) and a relatively small particle size of 0.2 μm. Again, good correlation is observed between the model prediction and the experimental measurements for a low particle concentration. As concentration increases, so does the tendency for global beam mode of deformation, and the experimental trend "falls off" the linear trend predicted by Eq. (30). At a particle concentration of about 10% and higher, the cell or strand bending dominate the response of the pad. This situation is depicted in Fig. 15. It is observed that MRR decreases with increasing particle size in this regime. The experimental trend correlates very well to the prediction obtained from the beam model [Eq. (32)].

Another set of experimental measurements, investigating the effect of abrasive particle size is carried out by Zhou et al. [15]. These experiments are carried on Struers Rotopol 35 polisher. The grooved IC1000 pad (supplied by Rodel, Inc.) is used in all the experiments. The abrasive particles have a very narrow particle size distribution with average particle diameters of 10, 20, 50, 80, 110, and 140 nm. The abrasive concentration was varied by diluting the 30 wt % concentration slurry with DI water to obtain 1, 5, 10, 15, 20, and 25 wt. %. The pressure was varied from 18 kPa to 45 kPa, and the table speed was varied from 0.4 m/s to 0.9 m/s. Similarly, the Preston constant is used as a fitting parameter for model prediction in Fig. 16 by fitting a single data point to get the scaling factor then use it for the entire data set.

Figure 16 shows the variation of MRR with particle size for relatively small particles (10–140 nm) at a relatively high concentration of 30 wt. % by weight. It is observed that the MRR initially increases with particle size, saturates at around particle size of 80 nm, and decreases with further increase in particle size. Zhou et al. [15] have conducted these experiments at three different operating pressures and velocities. The experimental data points are shown by symbols. The experimental trends are then compared to model predictions from two different regimes. It may be assumed that the pad undergoes local deformation at smaller particle sizes, and Eq. (30) is thus applicable at smaller particle sizes. At larger particle sizes, the pad undergoes global beam mode of deformation, thus Eq. (32) is applied in that regime. It is observed that the model predictions in both regimes fit the experimental trend very well.

4 Discussion and Concluding Remarks

A new mechanism for ductile material detachment from the parent surface based on scratch intersection is proposed in this paper, and applied to MRR prediction of CMP processes. This is a departure from existing MRR models, where it is assumed that a moving abrasive particle removes material all along its track. The present model assumes that material is plowed to the side (but not detached) along a particle's track. However, it is only detached when the deformation profiles of two tracks intersect each other at a favorable angle. The proposed scratch intersection model is physically motivated, and provides predictions for Preston constants with the same order as those measured experimentally for CMP of copper (Figs. 11 and 12). This is in contrast to existing practice where Preston constant has typically been used to fit the model predictions to experimental observations. To further realize the model utility of the scratch intersection concept, if one would compare any of the existing models that rely on the assumption of removal of materials along the entire track of the abrasive particle, then the predicted MRR would be about three order of magnitude higher than experimental measurements. Moreover, the scratch intersection model prediction of MRR variations with pressure and velocity are also very similar to observed experimental trends.

It has been observed in the literature (e.g., Refs. [15,17,18]) that under different conditions, the MRR may show an increasing or decreasing trend with increasing particle size and concentration. It is observed in our model developments that this apparent ambiguity is due to different regimes of slurry-pad interactions, which induce completely different deformation modes and its associated force partitioning in the CMP process. The proposed scratch intersection based CMP model delineates these different regimes of operation. It is noted that for soft pads subject to relatively small particle sizes and low particle concentrations, the pad undergoes a local deformation pattern where the abrasive particle indents the pad surface. The force partition associated with such a deformation mode causes increasing trend in MRR with increasing particle size and increasing particle concentration. As the particle size and concentration increases, the pad deformation mode changes from the local "indentation" deformation mode to more global deformation, where cells or strands on the pad surface deform globally by bending. In this regime of slurry-pad interaction, the nature of force partition changes, causing a decreasing trend in MRR with an increase in either particle size or particle concentration. The proposed scratch intersection models can capture both regimes, and the model predictions correlate quite well to experimental observations.

As predicted by the proposed scratch intersection model, the MRR trend with increasing particle size and concentration is seen to switch from an increasing trend to a decreasing trend as a critical value of particle size and concentration (relative to pad stiffness) is exceeded. Such a trend is clearly observed in the experimental data of Mahajan et al. [18]. The transition point also shifts depending on specific particle size and concentration. Determination of such transition points is the focus of our further research in this area.

The proposed model provide a handle on understanding the origin of the Preston constant and provides means to predict this constant as a function of the full process parameters, including detailed pad morphology, particle size and concentration, polished surface mechanical properties as well as the external control variables of applied pressure and relative velocities. Such detailed model would provide the means to explore the design space and optimize the process parameters. Moreover, by including the details of the pad morphology, one would be able to predict the performance degradation and generation of defects due to pad

wears and pore clogging. These issues are currently being addressed within the proposed framework of models.

Acknowledgment

This material is based upon work supported by the Carver Foundation, and the U.S. National Science Foundation Grant No. DMI-0084736. The authors gratefully acknowledge this support. Any opinions, findings, and conclusions or recommendations expressed in this material are those of the authors and do not necessarily reflect the views of the sponsoring agencies.

References

[1] Che, W., Guo, Y. Chandra, A. Bastawros, A.-F., 2003, "Mechanistic understanding of material detachment during micro-scale polishing", ASME J. Manuf. Sci. Eng., **125** No. 4, pp. 731–735.
[2] Preston, F. W., 1927, "The theory and design of plate glass polishing machine," J. Soc. Glass Technol., **11**, No. 44, pp. 214–256.
[3] Luo, J. and Dornfeld, D. A., 2001, "Material removal mechanism in chemical mechanical polishing: Theory and modeling," IEEE Trans. Semicond. Manuf., **14**, No. 2, pp. 112–133.
[4] Fu, G., Chandra, A., Guha, S., and Subhash, G., 2001, A plasticity based model of material removal in chemical mechanical Polishing (CMP), IEEE Trans. Semicond. Manuf., **14**, No. 4, pp. 406–417.
[5] Bastawros, A.-F., Chandra, A., Guo, Y., and Yan, B., 2002, "Pad Effects on Material Removal Rate in Chemical Mechanical Planarization," J. Electron. Mater., **31**, No. 10, SPEC., pp. 1022–1031.
[6] Seok, J., Sukam, C. P., Kim, A. T., Tichy, J. A., and Cale, T. S., 2003, "Multiscale material removal modeling of chemical mechanical polishing," Wear, **254**, pp. 307–320.
[7] Shaw, M. C., 1984, *Metal Cutting Principles*, Clarendon, Oxford.
[8] Che, W., 2002, "A Study on Material Detachment Mechanism in the CMP Process," Master's thesis, Iowa State University, Department of Mechanical Engineering.
[9] Kuehn, J., 2000, "Particle scale and wafer scale effects in Chemical and Mechanical Planarization (CMP)," M.S. thesis, Department of Mechanical Engineering and Engineering Mechanics, Michigan Technological University.
[10] Lange, K. and Kurz, N., 1984, "Theoretical and experimental investigation of the 'Groz' cold shape-rolling process," Inst. for Metal Forming Report, University of Stuttgart, Germany.
[11] Chandra, A., 1989, "Profile rolling of gears: a boundary element analysis," ASME J. Eng. Ind., **111**, pp. 48–55.
[12] Xie, Y, and Williams, J. A., 1993, "The generation of worn surfaces by the repeated interaction of parallel grooves," Wear, **162-164**, pp. 864–872.
[13] Cook, L. M., 2000, "Chemical Mechanical Polishing in Silicon Processing," *Semiconductors and Semimetals*, Academic, San Diego, CA, Vol. 63, pp. 156–166.
[14] Gouda, S. D., Bastawros, A.-F., and Chandra, A., 2003, "Multiscale characterization of pad role on material removal rate in CMP," Mater. Res. Soc. Symp. Proc., **767**, pp. 95–100.
[15] Zhou, C., Shan, L., Hight, R., Danyluk, S., Ng, S. H., and Paszkowski, A. J., 2002, "Influence of colloidal abrasive size on material removal rate and surface finish in SiO2 chemical mechanical polishing," Lubr. Eng., pp. 35-41.
[16] Ouma, D. O., 1998, "Modeling of chemical mechanical polishing for dielectric planarization," Ph.D. thesis, Massachusetts Institute of Technology, Department Electrical Engineering and Computer Science.
[17] Luo, Q., Ramaranjan, J. S., and Babu, S., 1998, "Modification of the Preston equation for the chemical-mechanical polishing of copper," Thin Solid Films, **335**, pp. 160–167.
[18] Mahajan, U., Bielmann, M., and Singh, R. K., 1999, "Abrasive Effects in Oxide Chemical Mechanical Polishing," Mater. Res. Soc. Symp. Proc., **566**, pp. 27–32.